Exhumation History along the Muli Thrust -Implication for Crustal Thickening mechanism in Eastern Tibet

Paul Pitard, Anne Replumaz, Marie-Luce Chevalier, Philippe-Hervé Leloup, Mingkun Bai, Marie-Pierre Doin, Cédric Thieulot, Xiong Ou, Mélanie Balvay, Haibing Li

Exhumation History along the Muli Thrust –

Implication for Crustal Thickening mechanism in Eastern Tibet

Paul Pitard[1], Anne Replumaz[1], Marie-Luce Chevalier[2,3], Philippe-Hervé Leloup[4], Mingkun Bai[2], Marie-Pierre Doin[1], Cédric Thieulot[5], Xiong Ou[1], Mélanie Balvay[1], Haibing Li[2,3]

[1] Univ. Grenoble Alpes, CNRS, USMB, IRD, IFSTTAR, ISTerre, 38000 Grenoble, France.

[2] Institute of Geology, Chinese Academy of Geological Sciences, 26 Baiwanzhuang Road, Beijing 100037, People's Republic of China.

[3] Southern Marine Science and Engineering Guangdong Laboratory (Guangzhou), Guangzhou 511458, People's Republic of China

[4] Laboratoire de Géologie de Lyon, CNRS UMR 5570, Université de Lyon 1, 69622 Villeurbanne, France.

[5] Mantle Dynamics and Theoretical Geophysics, Utrecht University, The Netherlands

Corresponding author: Paul Pitard (paul.pitard@univ-grenobles-alpes.fr)

Key Points:

• Thermo-kinematic modelling of Muli thrust, a major thrust fault of SE Tibetan Plateau.

• ~15 km crust exhumation in 50 Ma on a high-angle (<70°) ramp - décollement fault linked to thickening of SE Tibetan crust.

• Fault related to significant Moho step and shear wave velocity contrast in deep crust suggests entire crust implication

Citation: Pitard, P., A. Replumaz, M.-L. Chevalier, P.-H. Leloup, M. Bai, M.-P. Doin, C. Thieulot, X. Ou, M. Balvay, and H. Li, Exhumation History Along the Muli Thrust—Implication for Crustal Thickening Mechanism in Eastern Tibet, GRL, 48, doi: 10.1029/2021GL093677, 2021

Abstract

Thrusting implication in the crustal thickening history of eastern Tibet is highly debated. The ~250 km-long Muli thrust of the Yalong thrust belt in SE Tibet is a major Miocene structure with a pronounced topographic step (~2000 m). Using thermo-kinematic modelling based on thermochronology data, we constrain the crustal geometry of the thrust as being steep (>70°) at the surface, in agreement with field observations, and flattening at depth (≥20 km) on an intra-crustal décollement. Thrusting motion on the fault shows a velocity of 0.2 ± 0.06 km/Ma since 50 Ma, followed by an acceleration at a rate of 0.6 ± 0.08 km/Ma starting at 12.5 ± 1 Ma, yielding a total of ~15 km of exhumed crust. Deeper, deformation may be localized through a ductile shear zone, and be related to the ~15 km Moho step and shear wave velocity contrast imaged by tomography beneath the Yalong thrust belt.

Plain language summary

The India-Eurasia collision (~50 million years ago [Ma]) led to the formation of the Tibetan Plateau, the world's largest and highest orogenic plateau. The formation and evolution of such a unique geological feature has been one of the main controversies in Earth Sciences for decades, especially regarding the role of faulting in the thickening of the crust. Here, we present 3D thermo-kinematic models of thermochronology data allowing to constrain the exhumation history of the Muli thrust fault, a ~250 km-long major structure of the SE Tibetan margin, linked to significant steps in surface topography and in crustal boundary at depth (Moho). We constrain a steep fault (>70°) within the upper crust, consistent with field observations, that flattens at depth (≥20 km). The Muli thrust presents rapid thrusting motion (0.6 ± 0.08 km/Ma) that initiated at ~12.5 Ma, following a slower phase (0.2 ± 0.06 km/Ma) since 50 Ma, with total rock exhumation of ~15 km. This underlines the important role of thrust faulting in the thickening of the SE Tibetan crust.

1. Introduction

The eastern margin of the world's largest and highest orogenic plateau, the Tibetan Plateau, shows contrasted edges, with a steep topographic gradient along the Longmen Shan (LMS) north of the Xianshuihe strike-slip fault (XF), and gentler slopes across the Yalong margin to the south (Figure 1a). The driving mechanism(s) leading to such contrasts between margins are still poorly understood and have given rise to end-member models of plateau growth with different crustal structures: either a weak lower crust localizing crustal thickening ('channel flow model', e.g. Clark & Royden, 2000), or a more rigid crust, with thickening that includes the upper crust, in a brittle manner ('stepwise model', Tapponnier et al., 2001). Those two end-member models can be tested by investigating the role of thrusting mechanisms in SE Tibet.

At present, upper crustal deformation of the LMS is dominated by reverse faulting with a small component of right-lateral motion, as shown by recent earthquake focal mechanisms such as that of the 2008 Mw7.9 Wenchuan earthquake (e.g., Fielding et al., 2013; de Michele et al., 2010). This event ruptured two subparallel reverse structures, the Guanxian and Beichuan thrusts (Figure 1b), with steep shallow ramps (up to 70°) which root between 15 and 25 km-depth on a sub-horizontal décollement zone (e.g., Airaghi et al., 2017; Fielding et al., 2013; Hubbard & Shaw, 2009; Li et al., 2013; Qi et al., 2011) corresponding to the brittle-ductile transition (Feng et al., 2016). In addition, receiver function profiles (Robert et al., 2010) and regional shear waves tomography images (Yao et al., 2008) show a ~20 km step of the Moho depth between the plateau (~60-63 km) and the Sichuan craton (~40 km) at the apex of the Wenchuan shear zone. This has been interpreted either as a lower crustal ductile continuation of the shear zone (Robert et al., 2010), or as the halt of the lower crustal flow by the rigid Sichuan craton, hence inducing upward motion along the thrusts (Burchfiel et al., 2008).

By contrast, the Yalong margin only shows normal and strike-slip focal mechanisms, as well as two active left-lateral strike-slip fault systems: XF (Allen et al., 1991) and Litang (Chevalier et al., 2016; Wang & Burchfiel, 2000). Major geologic discontinuities attest, however, to the presence of the NE to EW-trending Yalong thrust belt (YTB) along the margin (e.g., Clark et al., 2005; Liu-Zeng et al., 2008; Perrineau, 2010; Wang & Burchfiel,

2000), consisting of the Muli and Jinhe-Qinghe thrusts that merge south of the XF (Figure 1b). Being most likely currently inactive considering regional seismicity, these thrusts were however active during the Miocene, as shown by thermochronology ages (Clark et al., 2005) as well as by the significant topographic step (~2000 m) (Figure 1c). The YTB has been identified as the SW continuation of the LMS (Yan & Lin, 2015) prior to activation of the XF at ~9 Ma (Zhang et al., 2017), although the amount of thrusting remains controversial. Similarly to what has been observed in the LMS, tomography images (Yao et al., 2008) reveal a ~15 km vertical jump in crustal thickness across the YTB between the plateau (~60-63 km) and the Yalong margin (45-50 km) (Figure S5), coinciding with the limit of a low shear velocity layer in the middle and lower crusts (Figure S6), suggesting that the YTB plays a major role in thickening of the Yalong margin. By contrast, the channel flow model predicts a mainly horizontal flow at depth across the Yalong margin, generating a smooth topographic gradient with no spatial discontinuity and no thickening of the upper crust (Clark & Royden, 2000). Whether the Yalong margin has been uplifted by major thrusts or has only been passively uplifted, is therefore key to understand the processes involved in the formation of SE Tibet and distinguish between these models. In this paper, we focus on the structure, amount and timing of exhumation of the Muli thrust, the northernmost segment of the YTB. We use thermo-kinematic modelling of low-temperature thermochronology data with apatite and zircon (U-Th)/He (AHe and ZHe respectively), and apatite fission-track (AFT) ages, as well as high-temperature systems with $^{40}Ar/^{39}Ar$ on biotite (BAr) and muscovite (MAr) from the hanging wall.

In this paper, we focus on the structure, amount and timing of exhumation of the Muli thrust, the northernmost segment of the YTB. We use thermo-kinematic modelling of low-temperature thermochronology data with apatite and zircon (U-Th)/He (AHe and ZHe respectively), and apatite fission-track (AFT) ages, as well as high-temperature systems with $^{40}Ar/^{39}Ar$ on biotite (BAr) and muscovite (MAr) from the hanging wall.

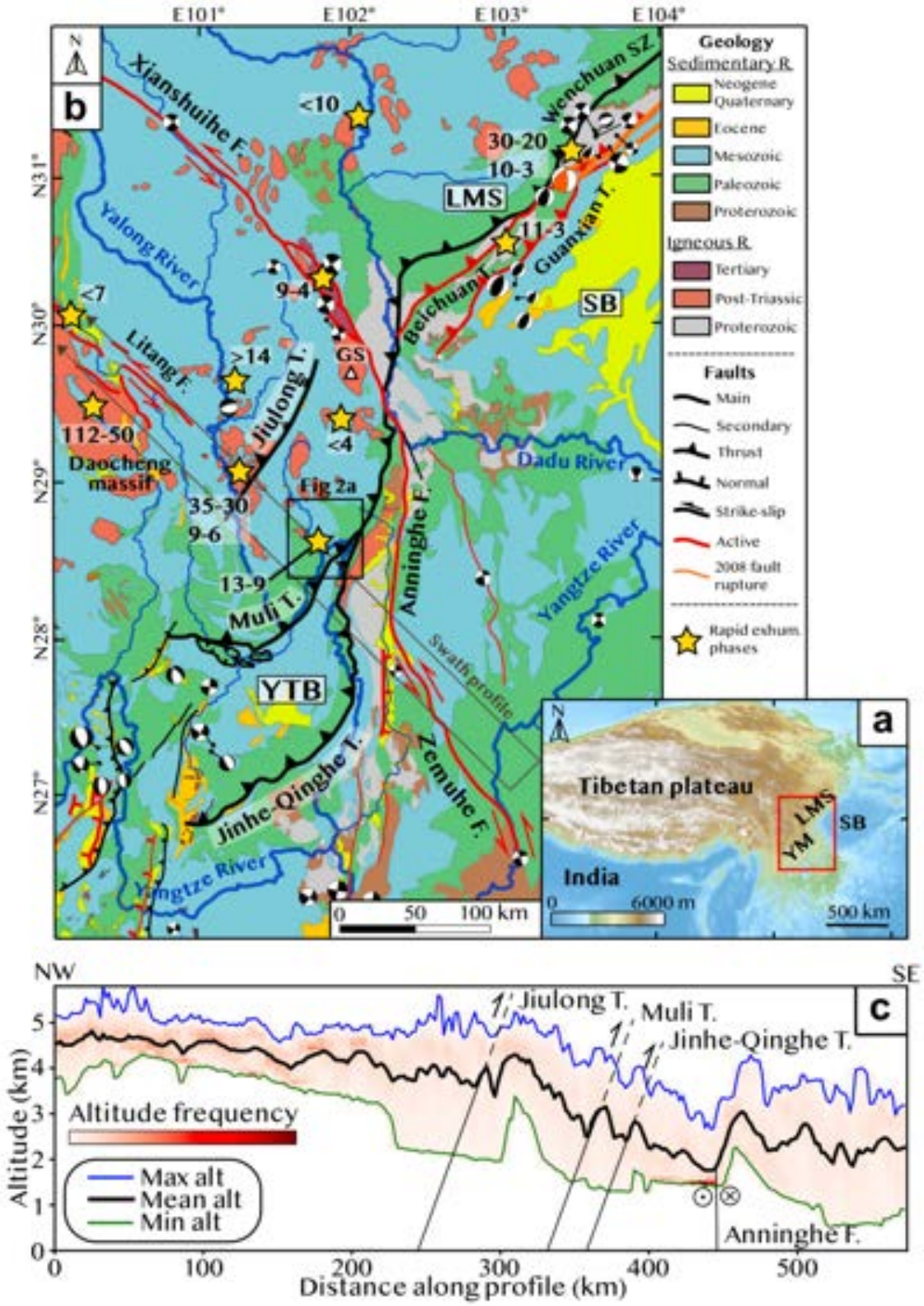

Figure 1: *(**a**) Topographic map of Tibet (YM: Yalong Margin, LMS: Longmen Shan, SB: Sichuan Basin). (**b**) Geologic map of SE Tibet (CIGMR, 2004) with Mw>5 earthquake focal mechanisms, including 2008 Wenchuan earthquake (Mw7.9) in orange (Global CMT catalog). YTB: Yalong thrust belt, SZ: shear zone, GS: Gongga Shan. (**c**) Swath elevation profile across YTB.*

2. Geological setting and timing of exhumation

The NW-dipping Muli thrust runs southward for ~250 km from the XF, with mainly Paleozoic resting atop Mesozoic rocks (Figure 1b). The thrust corresponds to a large topographic step bounding to the east the low-relief, high (>4000 m) Tibetan Plateau, as well as a sharp bend of the Yalong River (Figure 1). There, the hanging wall consists of schists and marbles, mapped as Paleozoic and Triassic, with NNW to W-trending folds, with N70-130°-trending schistosity, intruded by numerous Cretaceous granites such as that of Datan (Figure 2a). Along the mapped trace of the thrust, schists and marbles have a strong schistosity and foliation trending N30° and steeply dipping 76°W on average, within a ~2 km-wide zone. Locally, the schistosity has a sigmoid geometry with slightly shallower (74°W) shear planes indicative of reverse shear (Figure 2b). In the footwall, sediments are mapped as Triassic and Upper Paleozoic and are only intruded by one small Mesozoic granite (Figure 1b).

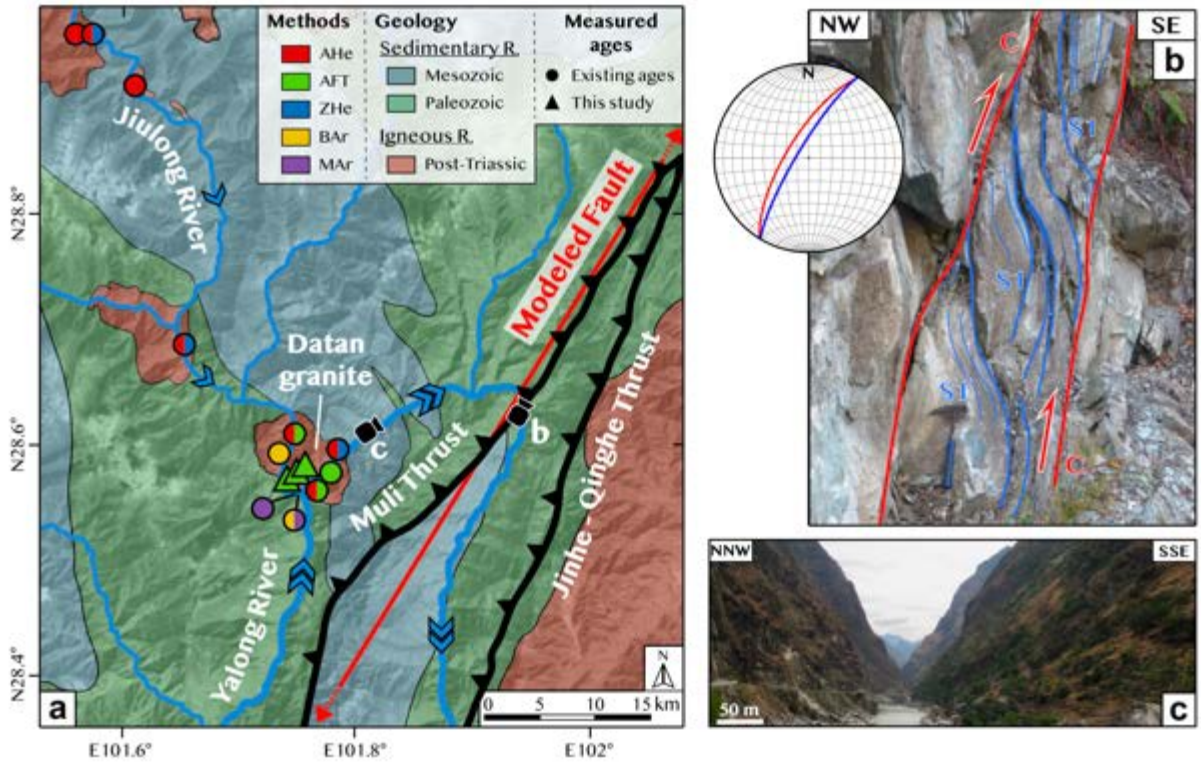

Figure 2: *(**a**) Geologic map of Yalong River bend region (CIGMR, 2004), atop Landsat image, with sample locations. (**b**) Outcrop along Muli fault and stereographic plot (inset) showing sigmoidal schistosity (S1) between steep shear planes (C) indicating reverse shear. (**c**) Photo of deeply incised Yalong River.*

Published AHe and AFT ages in the hanging wall of the Muli thrust have been interpreted as indicating fast exhumation between 9 and 13 Ma (Clark et al., 2005), while 80 km NW of the Muli thrust, AHe and ZHe ages have been interpreted to indicate the reactivation of the Jiulong thrust between 6 and 9 Ma, after an initial rapid exhumation phase between 35 and 30 Ma (Zhang et al., 2016). In the Gongga Shan massif, AFT and ZFT ages have been interpreted as representing the local activation of the XF at 9 Ma and its southward propagation along the Anninghe/Zemuhe fault at ~4 Ma (Zhang et al., 2017).

3. Results

3.1. Thermochronology data

Because of the steep banks of the Yalong River (Figure 2c), and the lack of granite outcrops in the footwall, the existing dataset is limited to valley bottoms in the hanging wall of the Muli thrust. We here add three samples along a steep profile between 1590 and 1873 m of elevation within the Datan granite (Figure 2a), which yield AFT ages of 4.1 ± 0.9, 5.0 ± 0.6 and 8.8 ± 0.9 Ma (Figure 3, Table S1 and Text S1). To best constrain the crust's cooling history using thermochronology dating, one needs an adequate spatial distribution of the data and the use of several distinct thermochronology systems. We therefore compile all available ages (seven AHe, three AFT, three ZHe, two BAr and two MAr) from previous studies (Clark et al., 2005; Perrineau, 2010; Wallis et al., 2003) (Table S2 and Text S2). Samples are ideally distributed along a 50 km-long transect perpendicular to the Muli thrust following the Jiulong River, at elevations between 1557 and 2624 m (Figure 2a). AHe (4.1 ± 0.2 to 13.9 ± 0.8 Ma) and ZHe ages (13.2 ± 0.8 to 37.2 ± 2.2 Ma) show a positive correlation with elevation and distance away from the fault (Figure 3). AFT ages are all located close to the junction between the Jiulong and Yalong Rivers (Figure 2a) and are tightly distributed between 4.7 ± 1.3 and 6.4 ± 1.1 Ma (Figure 3). BAr and MAr ages are Cretaceous, ranging from 104.3 ± 1.4 to 136 ± 7 Ma.

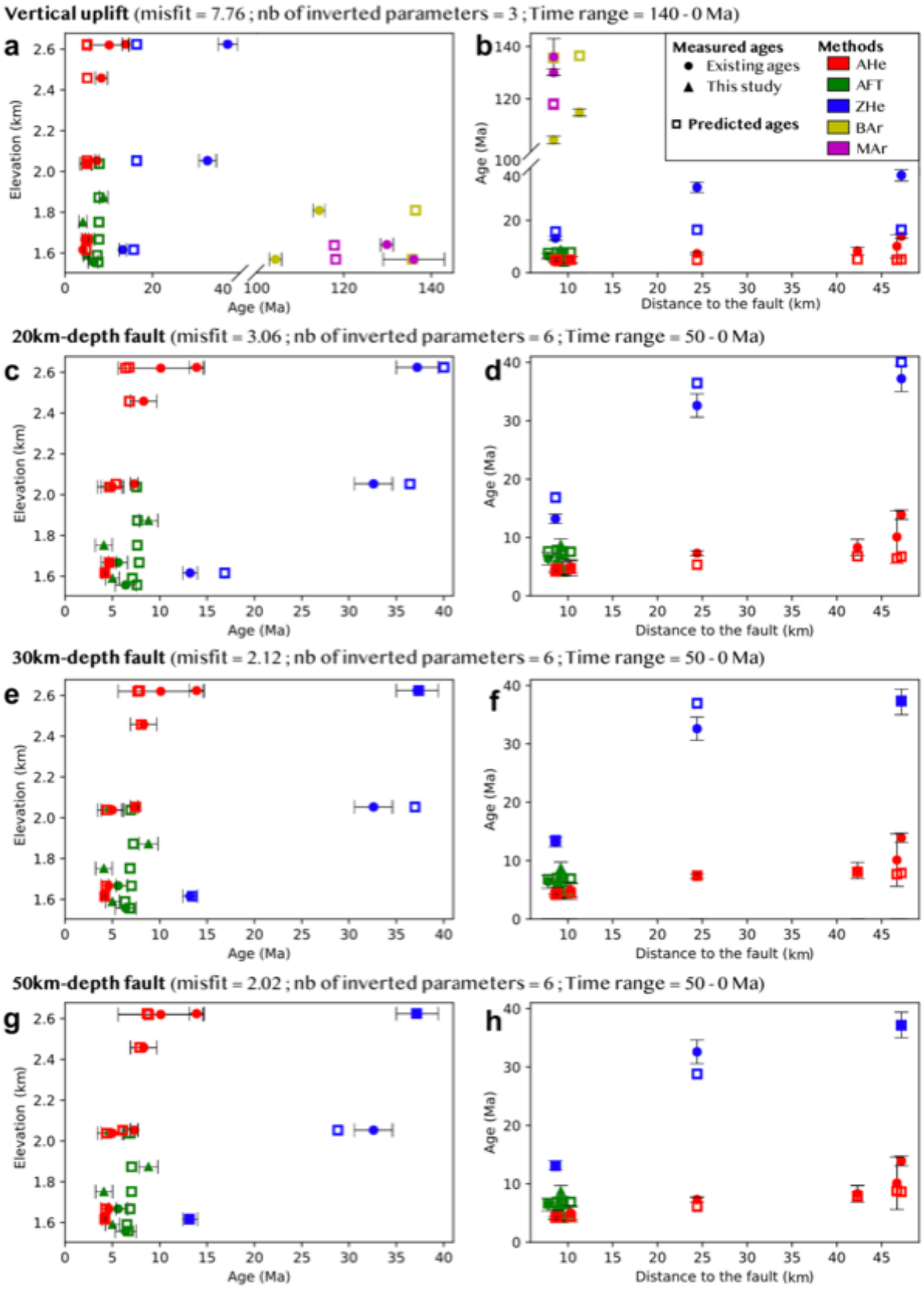

Figure 3: *Comparison between measured and predicted ages on vertical* ***(a,c,e,g)*** *and horizontal* ***(b,d,f,h)*** *profiles perpendicular to the Muli fault for different scenarios.*

3.2. Thermo-kinematic modelling

We use the code PECUBE (Braun, 2003; Braun et al., 2012) to unravel the 3D temporal evolution of the crust's thermal history. This code was designed to calculate theoretical ages for various thermochronometers, yielding the misfit value (equation S1) with the measured ages for different scenarios, and to use an inversion method to find the model with the lowest misfit value. We define a ~100 x 100 x 50 km block with present-day surface topography and set a basal temperature of 800 °C, corresponding to a geothermal gradient of ~ 35 °C/km (Clark et al., 2005; Zhang et al., 2015) (Tables S3, S4, and text S3).

4. Crustal thermal history driven by vertical exhumation

We first conduct an inversion with more than 3000 models (Table S3) to find the best fitting model that constrains the exhumation history for a scenario with a homogeneous vertical rock uplift. Our model starts at 140 Ma, slightly earlier than our oldest $^{40}Ar/^{39}Ar$ age. The best fitting exhumation scenario (misfit = 7.76) is a two-stages history with a first stage having a denudation rate of 0.033 km/Ma, followed at 14 Ma by a second stage with a faster rate of 0.47 km/Ma (Figure S1). This yields a total exhumation of 10.7 km since 140 Ma, including 6.5 km since 14 Ma. Predicted AHe ages are consistent with those measured for the low-elevation samples located <10 km away from the fault trace, while the four samples located at higher altitude, i.e., farther away from the fault, show predicted AHe ages that are much younger (up to ~5 Ma) than the measured ones (Figures 3a-b). The difference is even higher for the three ZHe predicted ages, i.e., up to ~15 Ma younger for samples farther from the fault. Those large differences suggest that a scenario with a homogeneous vertical uplift, and thus no fault, cannot fit the spatial distribution of our thermochronology dataset (Figures 4a-b).

4.1. Crustal thermal history driven by the Muli thrust

To simulate a more complex uplift velocity field, we implement a fault with exhumation of a hanging wall with respect to a stable footwall. The fault trace at the surface follows that of the Muli thrust (Figure 2a), and the number of segments defining the fault

geometry at depth is set to three, which appears sufficient to get a satisfying velocity field. Given the lack of geophysical data constraining the deeper part of the fault, we run three distinct inversions in which we fix the deepest segment to be horizontal at depths of 20, 30 and 50 km. We add three variables to invert, in order to define the Muli thrust geometry, and only consider the low-temperature data (AHe, AFT, ZHe, ages <40 Ma), removing $^{40}Ar/^{39}Ar$ ages to reduce the number of thermochronometers used, and the time window of 50 Ma, which allows to reach a well-constrained inversion by running twice as many models (>6000) than in our previous vertical exhumation setting.

The lowest misfit (2.02) inversion model is obtained for a steep (~80°) shallow fault segment down to 46 km-depth and a transitional segment from 46 to 50 km-depth dipping at ~10°, which joins the deep horizontal segment at 50 km-depth (Figures 4g-h). With this geometry, we find that the best fitting exhumation scenario occurred in two stages: a first stage with a fault velocity rate of 0.26 km/Ma, followed at 11.5 Ma by a second stage with a faster rate of 0.52 km/Ma (Figure S4). The modeled fault geometry yields an age zonation parallel to the fault, with young ages close to the fault, rapidly becoming older away from it (Figure 4). Young ages result from rapid vertical rock uplift above the steeply dipping fault plane, while away from the fault, older ages result from a slower rock uplift above the gently-dipping fault plane at depth. This thermo-kinematic model successfully reproduces the positive correlation between AHe and ZHe ages and distance to the fault (Figure 3g-h), with predicted AHe ages falling within uncertainty of the measured ones, and predicted ZHe ages evolving almost linearly with distance to the fault, reproducing well the measured ages. This spatial distribution is not obtained in our vertical exhumation scenario, and highlights the mandatory role of a listric Muli thrust.

Nevertheless, while the first order geometry of the fault is well constrained, the depth of the deep, flatter segment (equivalent to a basal décollement) is not. Indeed, running a model with a basal décollement at 30 km results in a misfit value being only slightly higher (2.12) than in our previous model using a basal décollement of 50 km (2.02). In that case, the shallow fault segment is dipping at 68°, the transitional segment is sub-horizontal (dip of 3°) (Figures 4e-f), and the transition time occurs 2 Ma earlier (13.5 Ma), separating two exhumation phases with velocity rates on the fault nearly identical to those in our previous model (0.24 and 0.54 km/Ma) (Figure S3). The predicted AHe ages in such a scenario are slightly younger than those predicted for the 50-km basal depth model, while the ZHe ages show a more pronounced break in slope with distance to the fault, also consistent with the

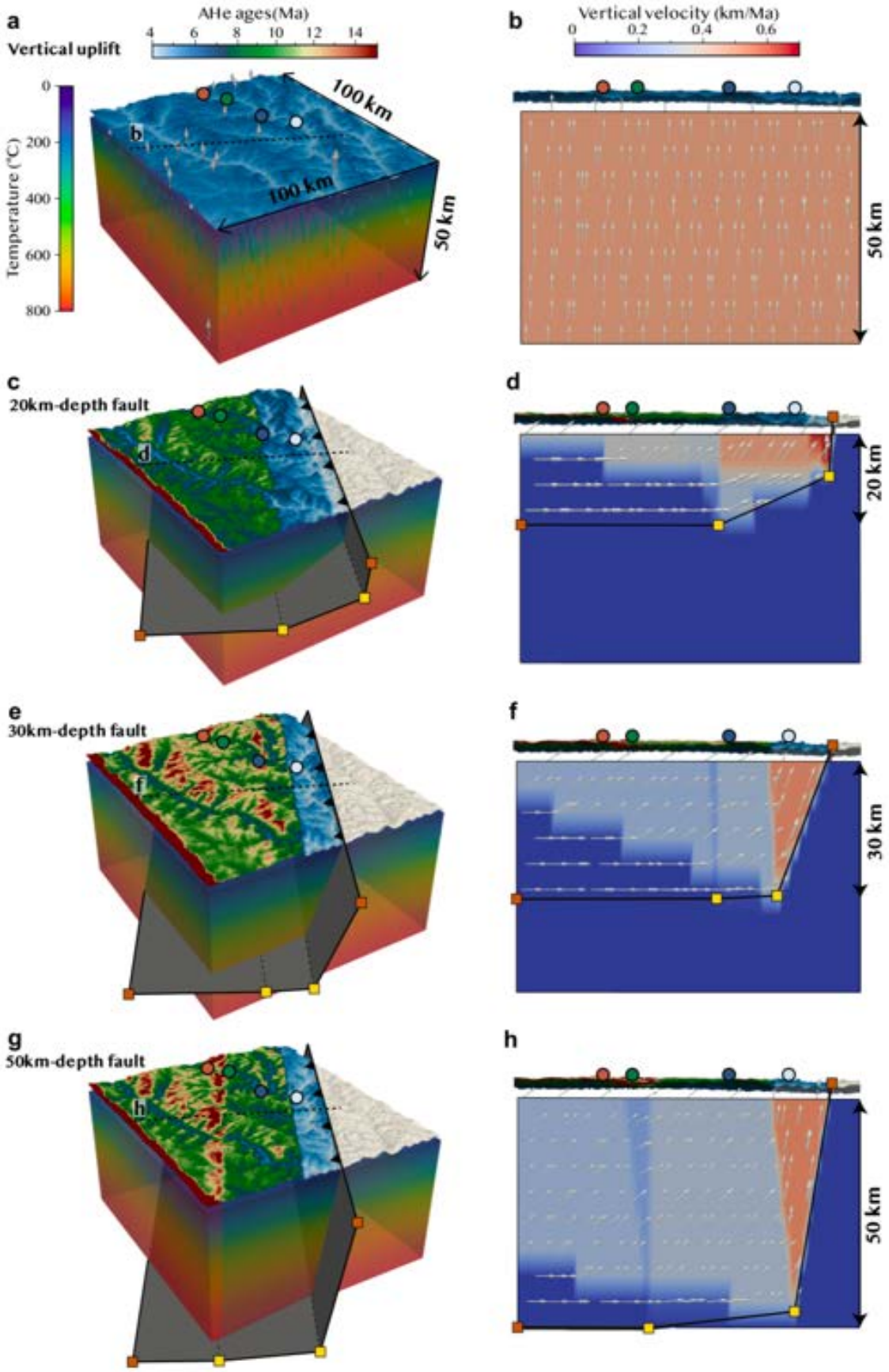

Figure 4: *Crustal thermal models for different scenarios overlaid by predicted present-day AHe ages wrapped on topography, with circles showing measured ages. Squares represent*

*inflexion points defining fault geometry (yellow: inverted points; orange: fixed points): (**a,c,e,g**) 3D view, (**b,d,f,h**) 2D rock particle velocities (arrows) along middle section during most recent exhumation phase.*

measured ages (Figures 3e-f). The misfit value (3.06) significantly increases for a model with a basal décollement depth of 20 km. In that case, the shallow fault segment is sub-vertical (~85°) down to 9 km-depth, the transitional segment is less steep (25°) from 9 to 20 km-depth (Figures 4c-d), and the transition time is 12.7 Ma, with a more pronounced rate jump from 0.14 to 0.67 km/Ma (Figure S2). The predicted AHe ages are ~2 Ma younger than the measured ones, and the predicted ZHe ages are up to 4 Ma older than the measured ages, leading to a higher misfit than in the previous models (Figures 3c-d).

4.2. Implication for the crustal thickening history of Eastern Tibet

Using both vertical and horizontal thermochronology data profiles in the hanging wall of the Muli thrust, we show that a scenario with a spatially homogeneous vertical uplift is incompatible with the currently available thermochronology dataset. A more complex velocity field driven by a high-angle ramp – flat décollement fault geometry is required (Figure 4). Using data inversion, we obtain a ramp that dips between 85 to 68°, in agreement with surface field observations (Figure 2b), as well as with the high-angle (70°) ramp imaged in the LMS, for décollement depths of 20, 30 and 50 km that we test in agreement with LMS observations (Feng et al., 2016; Fielding et al., 2013; Li et al., 2013; Qi et al., 2011; Robert et al. 2010). The upper crustal velocity field in all three models show similar general kinematics with nearly vertical motion close to the fault leading to young predicted ages, and a more oblique, slower velocity farther away from the fault yielding older predicted ages, consistent with the measured ages (Figure 3). The exhumation evolution is also very similar between the three models, with a slow velocity rate on the fault between ~0.14 and ~0.25 km/Ma from 50 to 12.5 ± 1 Ma, followed by a rapid phase between ~0.53 and ~0.67 km/Ma. The early exhumation phase may be related to that recorded in the hanging wall of the Jiulong thrust between 35 and 30 Ma (Zhang et al., 2016), and to that in the LMS between 30 and 20 Ma (Tan et al., 2014; Wang et al., 2012). In the LMS, a second phase of rapid exhumation started at ~11 Ma at a rate of ~0.65 km/Ma (Godard et al., 2009), similar to the fast exhumation we document here along the Muli thrust. This would confirm a continuity between the YTB and

LMS prior to the activation of the XF at ~9 Ma, having since then offset them by ~60 km (Yan & Lin, 2015; Zhang et al., 2017) (Figure 1b).

For a thrust rooted at 20 km-depth, predicted ages are slightly diverging from the measured ages (younger predicted AHe ages, older ZHe ages, Figures 3c-d), leading to a slightly higher misfit (3.06) than for deeper décollements (2.02 to 2.12). Nevertheless, considering the simplicity of the kinematics modelling associated to fault displacement rates, such higher misfit is insufficient to reject this model, and mostly shows that low-temperature thermochonology data are more adequate to constrain the upper crust thermal evolution than that of the lower crust. To further discuss the structure of the Muli thrust in the lower crust, we then compare our results with geophysical data and crustal structures proposed for the LMS. The 20-km depth model agrees with the depth of the brittle-ductile transition (Feng et al., 2016), considering that thickening during the Cenozoic collision is limited to the brittle upper crust (Airaghi et al., 2017). The 50 km-depth model agrees with the thickening of the entire crust in the hanging wall of the Muli thrust fault (Figure 4h), as proposed for the Wenchuan shear zone in the LMS (Robert et al., 2010). This scenario is the only one compatible with an abrupt step of the Moho depth observed beneath the Yalong margin (Yao et al., 2008) (Figure 5). Indeed, for the Yalong margin, such step cannot be explained by a rheological contrast, as invoked in the LMS between the rigid Sichuan craton and the weak Tibetan crust, inducing a strong thickening of the Tibetan lower crust halted by the craton (e.g. Burchfiel et al., 2008). Beneath the Yalong margin, only a listric geometry of the Muli thrust rooting deep into the lower crust may induce a Moho step, the eastward limit of a low velocity crustal layer (Figure 5), and the thickening of the entire crust (Figure 4h). Below 20 km-depth, deformation has to be more ductile and localized in a ductile shear zone aligned with the upper crustal Muli thrust, which, since 50 Ma, exhumed a total of ~15 km of crust along its high-angle ramp and ~8 km above its sub-horizontal deep décollement, forming a significant topographic step of ~2 km (Figures 1c and 5).

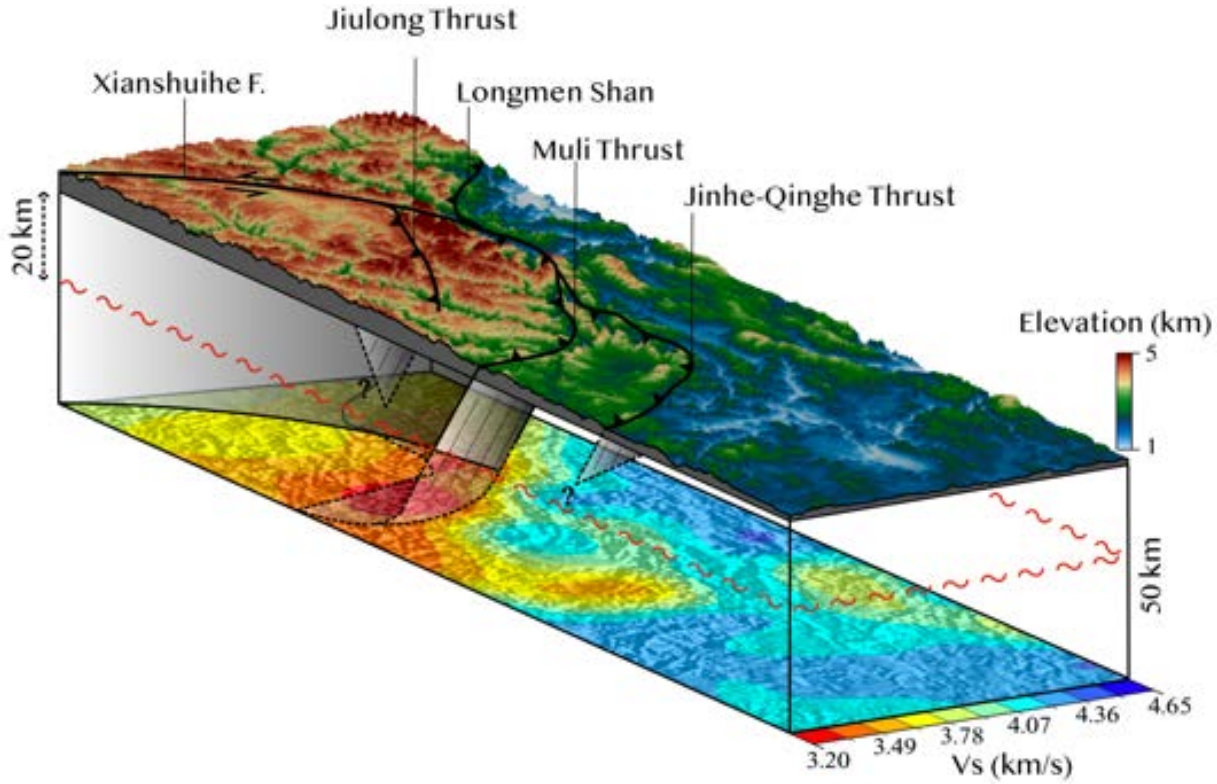

Figure 5: *3D block diagram of Muli crustal fault geometry showing surface topography (2x vertical exaggeration), 20 km-depth brittle-ductile transition ("~" symbol), and tomography section at 50 km-depth (Yao et al., 2008).*

5. Conclusion

We present 3D crustal models of different cooling scenarios using a wide spatial distribution of thermochronology ages from the Muli fault's hanging wall. We show that such a dataset can only be related to a complex velocity field generated along a high-angle (>70°) ramp thrust fault at the tip of a horizontal décollement. In such a scenario, we obtain a total exhumation of ~15 km since ~50 Ma, including ~7.5 km since 12.5 Ma. Our results show that the upper crust is strongly involved in the thickening of the Tibetan crust in this part of Tibet, and that it is not passively uplifted as assumed in channel flow models. Even if the rooting depth of the Muli fault remains difficult to constrain using such thermal modelling, tomography images reveal a Moho step and a shear wave velocity contrast in the deep lower crust at the apex of the YTB, which cannot be related to rheological contrast as proposed beneath the LMS. We therefore interpret such discontinuities as evidence of the listric nature

of the Muli thrust rooting deep into the lower crust, behaving as a ductile shear zone below 20 km-depth, allowing the thickening of the whole crust.

Acknowledgments

This work was supported by the TelluS Program of CNRS/INSU, ISTerre, LGL-TPE, Agence Nationale de Recherche (ANR “Tibetan Orchestra”), National Natural Science Foundation of China [NSFC 42020104007, 41941016] and the Second Tibetan Plateau Scientific Expedition of the Ministry of Science and Technology of China [2019QZKK0901].

Data statement

Supplementary data reported in this study are given in the supporting information and all apatite fission tracks data are stored in Figshare repository: https://doi.org/10.6084/m9.figshare.14770752. Supplementary thermochronology data used in this study can be found in Clark et al. (2005) (https://doi.org/10.1130/G21265.1) and Perrineau (2010) (http://www.theses.fr/2010GLOB0007).

Supplementary material

1. Apatite fission-track dating

Samples were irradiated in the FRM II Research Reactor at the Technical University of Munich (TUM). Samples were prepared and analyzed at the Institut des Sciences de la Terre (ISTerre) in Grenoble, and dated using the external-detector method (Hurford & Green, 1983). Calibration on six different standards (both Fish Canyon and Durango) allowed to define a zeta-calibration factor. Each sample yielded approximately 200 apatite grains. The best 19 grains (no inclusions, no cracks) were selected for measurement. Age estimates are provided using the binomFit program developed by M. Brandon (as described in Ehlers et al., 2005). In addition, χ^2-test has been used to assess the homogeneity of the AFT ages (Table S1).

2. Dataset

In addition to our data, we selected 11 samples with 17 measured ages (described below), dated with different thermochronometers: (U-Th)/He ages on apatites (AHe) and zircons (ZHe), apatite fission-track on apatite (AFT), and $^{40}Ar/^{39}Ar$ on biotites (Bar) and muscovites (Mar). Because of approximative elevations, we used those from Google Earth for each sample instead (Table S2).

<u>Wallis et al., 2003 samples</u>:

We selected three samples from the Datan granite with $^{40}Ar/^{39}Ar$ measurements on both muscovite and biotite. Both samples DHT-04 and DHT-09 show two different ages (ether plateau or weighted mean ages). For our modeling, we define a single BAr mean age of 115.4 ± 1.4 Ma for DHT-04 and a single MAr mean age of 129.8 ± 1.4 Ma for DHT-09.

<u>Clark et al., 2005 samples:</u>

Samples were collected during field campaigns in 1998 and 2001. For (U-Th)/He dating on apatite, three to five replicates were analyzed per sample. Mean ages are reported in Table S2. The 1-sigma error has been defined using the standard deviation of the replicate analyses divided by n-1 where n represents the number of replicates. For AFT analyses, a minimum of 22 grains were counted. Pooled ages are reported in Table S2.

Perrineau., 2010 samples:

Samples were collected within three different granitoid intrusions in the hanging wall of the Muli thrust. For each (U-Th)/He sample, a minimum of two replicates have been measured. On apatites, only sample KC 45 presents a mean age based on two replicates. Sample ages for KC 44 and KC 46 do not overlap because of inclusions. Only the younger age replicate has been used to define the final age. On zircons, a mean age has been defined for samples KC 44 with three replicates and KC 45 with two replicates. KC 46's final age is a single-grain age.

3. Thermo-kinematic modeling

Thirty meters ground resolution ASTER data were used to create a ~100x100 km digital elevation model (DEM) centered on thermochonology data. The resolution has to be lower to get an accurate number of calculations. DEM degradation has been done and give a horizontal resolution of 300 m. Input thermal parameters as well as NA parameterization are shown in Table S3. Isostatic compensation is limited to narrow river gorges and was estimated to be < 50 m in the SE margin of the Tibetan plateau (Clark et al., 2006). Isostatic rebound is known to be negligible on the plateau uplift and is thus omitted in our models. An important parameter is the default age where rock particles never reached the closure temperature (age given to rock that have not been reset). One way to define it is the use of thermochronology ages of high-elevated, low-erosional surface. For that, because of its proximity to the studied area, we used data from the Daocheng massif, defined by Clark et al. (2006) as a low-relief remnant surface. The Daocheng granitic massif presents (U-Th)/He ages on apatites from 50 to 112 Ma. The highest samples have ages between 91.4 and 111.9 Ma, that let us fix the specific default age at 100 Ma for our scenario with faults. In our scenario without faults, we fixed this default age at 140 Ma, slightly older than the oldest MAr age (136 Ma). Several tests have been conducted first to set the best NA parameters. A resampling ratio of 2/3 appears to be the best compromise in order to allow the inversion to converge, and to ensure a sufficient exploration of the parameter space. For each scenario, we ran several inversions covering a large field of possibilities, and improving the model step by step based on each inversion misfit value (Equation S1). This approach allowed to progressively reduce the parameters range window for each inversion and to test each parameter separately. This results in a precise model as shown by the Bayesian density of probability (Figures S1-S4). In our tectonic scenario, we used three different models which

differ in the maximal basal depth of the fault (20, 30 and 50 km). We present in Table S4 the lowest misfit inversion result for each parameter in different scenarios.

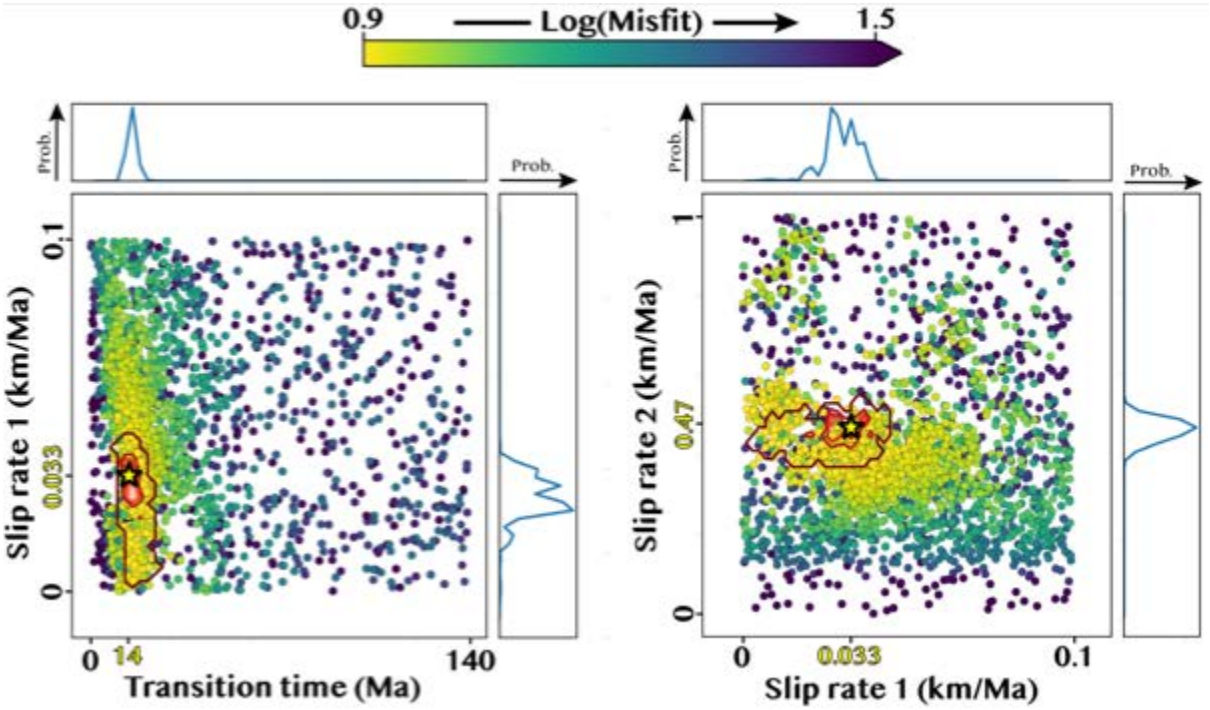

Figure S1. *2D scatter plots of inversion results for our vertical uplift scenario (without faults). One point corresponds to one tested model characterized by a misfit value represented by the color scale. Probability density function in one-dimension appears along the axes, and in 2D, it appears as red contour lines. The optimal solution is shown by the yellow star associated with its corresponding values.*

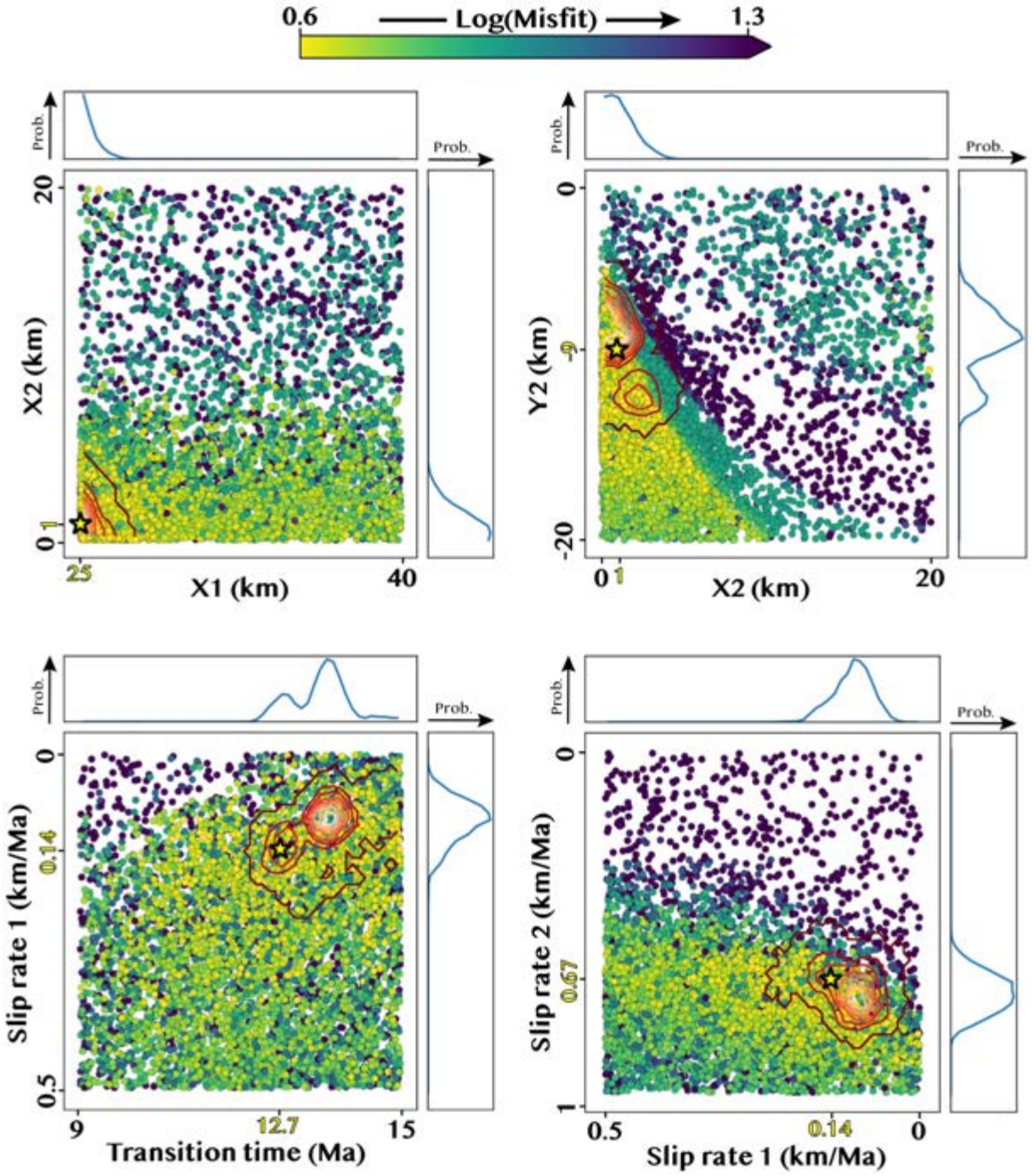

Figure S2*. 2D scatter plots of inversion results for our tectonic scenario with a fault rooted at 20 km-depth. (X,Y) are the coordinates of the inflection points defining the fault geometry. X represents the horizontal distance from the fault, and Y the depth. (X1,Y1) are the coordinates of the deepest inflection point, and (X2,Y2) are those of the shallowest one.*

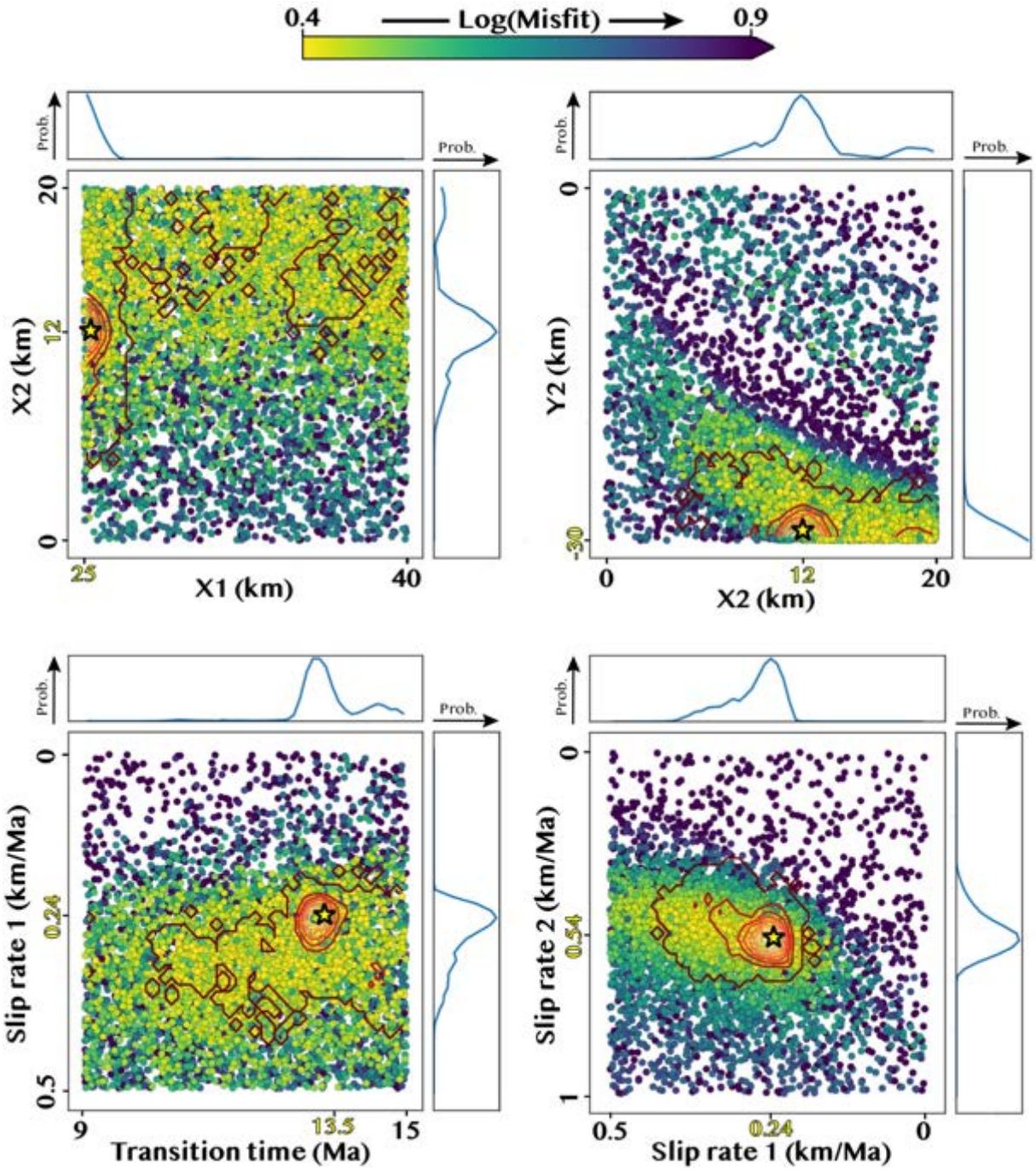

Figure S3. 2D scatter plots of inversion results for our tectonic scenario with a fault rooted at 30 km-depth.

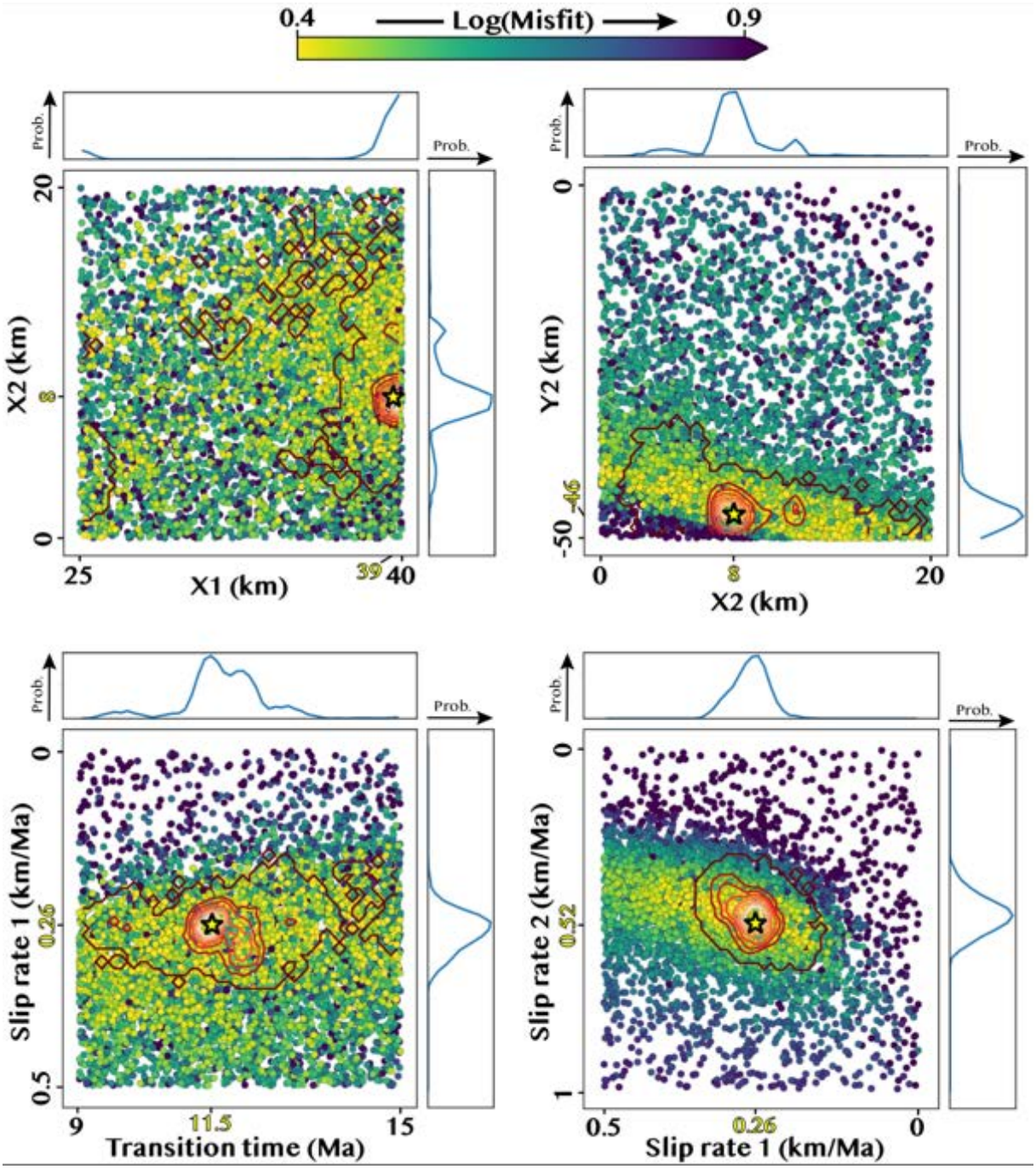

Figure S4*. 2D scatter plots of inversion results for our tectonic scenario with a fault rooted at 50 km-depth.*

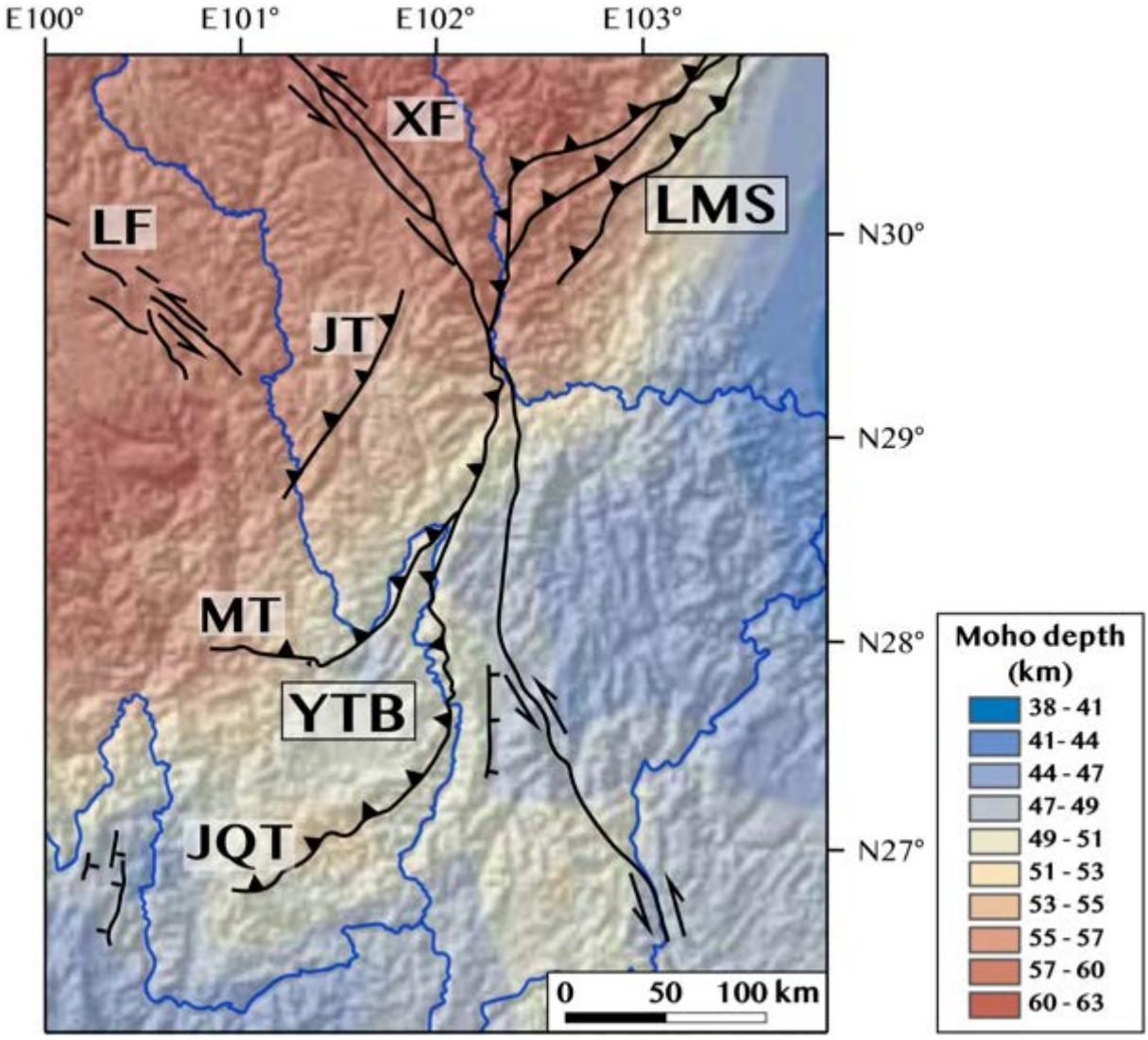

Figure S5*. Moho depth (modified from Yao et al., 2008). (XF = Xianshuihe Fault ; LMS = Longmen Shan ; LF = Litang Fault ; JT = Jiulong Thrust ; MT = Muli Thrust ; YTB = Yalong Thrust Belt ; JQT = Jinhe-Qinghe Thrust)*

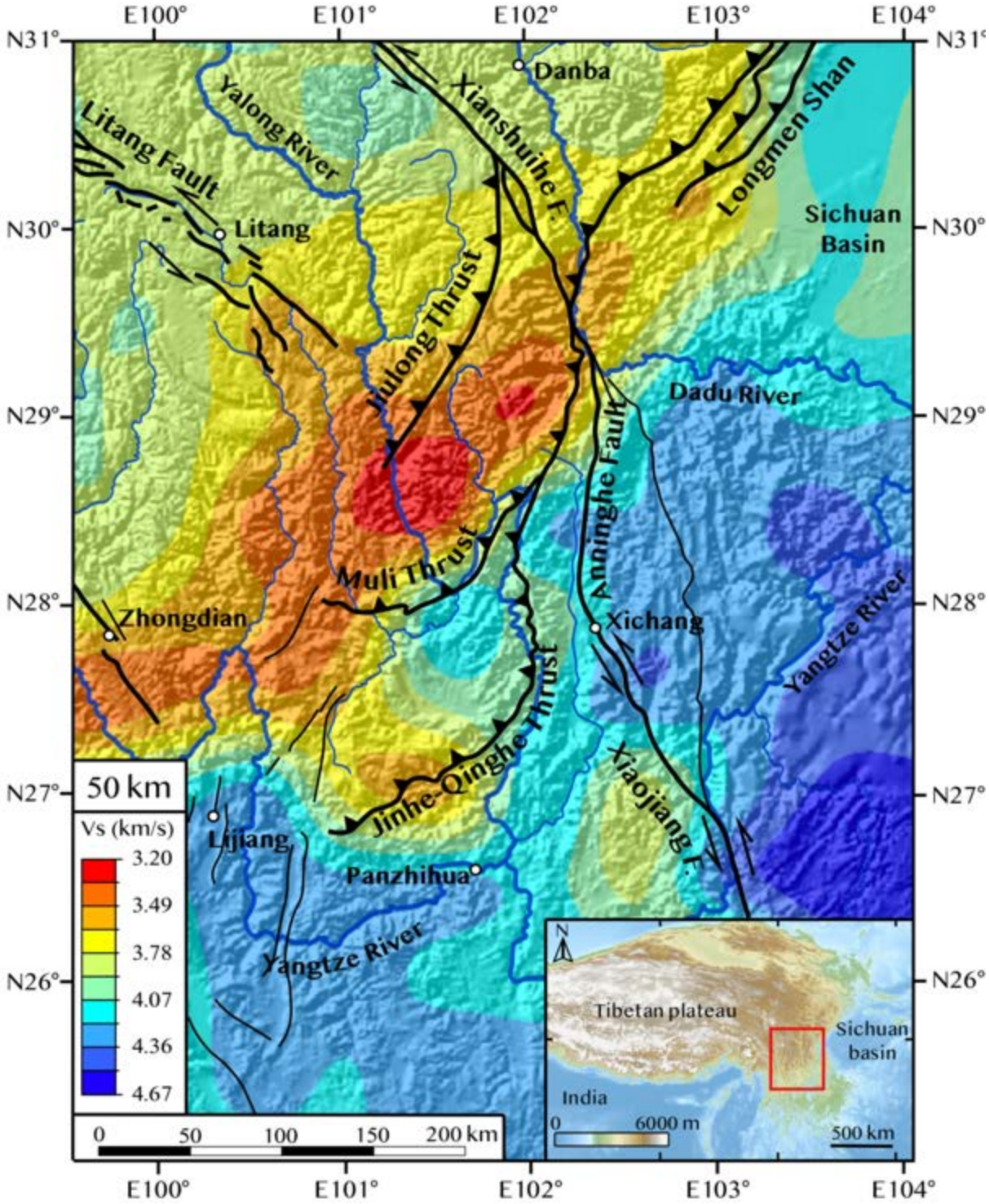

Figure S6*. 50 km depth shear wave speed (modified from Yao et al., 2008)*

Samples	Long E°	Lat N°	Elevation (m)	Nb Grain	Ns	Ni	U (ppm)	χ^2	Age (Ma) ± 1σ	Dpar (μm)
MU 14	101.73405	28.54014	1873	21	106	2109	19	97.9	8.8 ± 1.9	1.60
MU 15	101.73384	28.54236	1752	19	25	1084	13	55.9	4.1 ± 1.7	1.57
MU 16	101.73183	28.54069	1590	19	60	2116	24	79.7	5.0 ± 1.4	1.53

Table S1*. Results of apatite fission track (AFT) dating. Ns: Number of spontaneous tracks; Ni: Number of induced tracks; U: Uranium concentration;* χ^2 *: Chi-squared probability (%); Dpar: diameter of fission track etch pits.*

Samples	Reference	Long E°	Lat N°	Elevation (m)	AHe (Ma) ± 1σ	AFT (Ma) ± 1σ	ZHe (Ma) ± 1σ	BAr (Ma) ± 1σ	MAr(Ma) ± 1σ
MU 14	This study	101.73405	28.54014	1873		8.8 ± 1.9			
MU 15	This study	101.73384	28.54236	1752		4.1 ± 1.7			
MU 16	This study	101.73183	28.54069	1590		5.0 ± 1.4			
KC 44	Perrineau. 2010	101.7776	28.5619	1616	4.1 ± 0.2		13.2 ± 0.8		
KC 45	Perrineau. 2010	101.6434	28.6439	2053	7.3 ± 0.4		32.6 ± 2.0		
KC 46	Perrineau. 2010	101.5675	28.8747	2624	13.9 ± 0.8		37.2 ± 2.2		
MC-01-25	Clark et al. 2005b	101.7510	28.5425	1667	4.6 ± 0.8	5.6 ± 1			
MC-01-26	Clark et al. 2005b	101.7480	28.5342	1557		6.4 ± 1.1			
MC-01-27	Clark et al. 2005b	101.7335	28.5520	2038	5.0 ± 1.2	4.7 ± 1.3			
MC-01-29	Clark et al. 2005b	101.6034	28.8347	2458	8.3 ± 1.4				
MC-01-30	Clark et al. 2005b	101.5734	28.8742	2620	10.1 ± 4.5				
DHT-04	Wallis et al. 2003	101.7363	28.5722	1810				115.4 ± 1.4	
DHT-05	Wallis et al. 2003	101.7483	28.5338	1569				104.3 ± 1.4	136 ± 7
DHT-09	Wallis et al. 2003	101.7480	28.5335	1638					129.8 ± 1.4

Table S2*. Sample names and corresponding ages.*

Input thermal parameters	**Value**
Crustal thickness	50 km
Basal temperature	800 °C
Thermal diffusivity	25 km2/Ma
Temperature at sea level	25 °C
Atmospheric lapse rate	4 °C/km
Crustal heat production	10 °C/Ma
NA parametrization	**Value**
Number of iterations	10
Sample size for first iteration	350 (650)
Sample size for iteration	300 (600)
Number of re-sampling cells	200 (400)
Default age	140 (100) Ma

Table S3*. Thermal and NA parameters for PECUBE inversion. In parenthesis are the values related to our tectonic scenarios with a fault.*

Scenario	Tested parameters	Parameters range	Results	Misfit
Without a fault	Transition time (Ma)	140:0	14	7.76
	Exhumation rate 1 (km/Ma)	0:0.1	0.033	
	Exhumation rate 2 (km/Ma)	0:1	0.47	
With a fault rooting at 20 km-depth	Fault first inflection point coordinates (X2 ; Y2)	0:20 ; -20:0	1 ; -9	3.06
	Fault second inflection point coordinates (X1)	25:40	25	
	Transition time (Ma)	15:9	12.7	
	Velocity amplitude 1 (km/Ma) (Exhumation rate (km/Ma)	0:0.5	0.14 (0.14)	
	Velocity amplitude 2 (km/Ma) (Exhumation rate (km/Ma)	0:1	0.67 (0.67)	
With a fault rooting at 30 km-depth	Fault first inflection point coordinates (X2 ; Y2)	0:20 ; -30:0	12 ; -30	2.12
	Fault second inflection point coordinates (X1)	25:40	25	
	Transition time (Ma)	15:9	13.5	
	Velocity amplitude 1 (km/Ma) (Exhumation rate (km/Ma))	0:0.5	0.24 (0.22)	
	Velocity amplitude 2 (km/Ma) (Exhumation rate (km/Ma)	0:1	0.54 (0.5)	
With a fault rooting at 50 km-depth	Fault first inflection point coordinates (X2 ; Y2)	0:20 ; -50:0	8 ; -46	2.02
	Fault second inflection point coordinates (X1)	25:40	39	
	Transition time (Ma)	15:9	11.5	
	Velocity amplitude 1 (km/Ma) (Exhumation rate (km/Ma)	0:0.5	0.26 (0.26)	
	Velocity amplitude 2 (km/Ma) (Exhumation rate (km/Ma)	0:1	0.52 (0.51)	

Table S4*. Inverted parameters with tested range and lowest misfit value.*

Location	Rapid exhumation phases (Ma)	References
Dadu River	<10	Ouimet et al., 2010
Daocheng massif	112-50	Clark et al., 2005b
Gonggashan North	9-4	Zhang et al., 2017
Gonggashan South	<4	Xu and Kamp, 2000; Clark, 2003; Zhang et al., 2017
Jiulong thrust	35-30; 9-6	Zhang et al., 2016
Litang fault	<7	Zhang et al., 2015
Longmen Shan North	30-20; 10-3	Wang et al., 2012; Tan et al., 2014
Longmen Shan South	11-3	Godard et al., 2009
Muli thrust	13-9	Clark et al., 2005b
Yalong River	>14	Ouimet et al., 2010

Table S5*. Published rapid exhumation phases along major geological structures and rivers along the SE margin of Tibet*